In Situ Multiscale Study of Deformation Heterogeneities in Polylactide-Based Materials upon Drawing: Influence of Initial Crystallinity and Plasticization

Berit Brüster,[1] Arnaud Martin,[1] Julien Bardon,[1] Yao Koutsawa,[1] Sigrid Bernstorff,[2] Jean-Marie Raquez,[3] Stéphane André,[4] Philippe Dubois,[1] Frédéric Addiego[1]

[1]Department Materials Research and Technology (MRT) and National Composite Centre-Luxembourg (NCC-L), Luxembourg Institute of Science and Technology (LIST), ZAE Robert Steichen, 5 Rue Bommel, L-4940 Hautcharage, Luxembourg
[2]Sincrotrone Elettra Trieste, Strada Statale 14, AREA Science Park, Trieste 34149, Italy
[3]Laboratory of Polymeric and Composite Materials (LPCM), Centre d'Innovation et de Recherche en Matériaux Polymères (CIRMAP), Université de Mons, Place du Parc, 20, B-7000 Mons, Belgium
[4]Laboratoire d'Energétique et de Mécanique Théorique et Appliquée (LEMTA), Université de Lorraine, Ecole Nationale Supérieure d'Electricité et de Mécanique (ENSEM), 2 Avenue de la Forêt de Haye, TSA 60604, 54518 Vandœuvre Cedex, France
Correspondence to: F. Addiego (E-mail: frederic.addiego@list.lu)

Received 26 June 2018; revised 22 August 2018; accepted 22 August 2018; published online 23 September 2018
DOI: 10.1002/polb.24736

ABSTRACT: This work aims at identifying defects called deformation heterogeneities developing in polylactide (PLA)-based materials upon drawing at room temperature. The influence of the initial crystallinity and of the plasticization methodology (physical blending vs. reactive blending) on the type of defect is also investigated. Defects are characterized *in situ* by (a) calculating the volume strain from digital image correlation (DIC), (b) measuring their surface density from optical microscopy, and (c) assessing their scattering invariant from small-angle X-ray scattering. Complementary structural analyses are done by microcomputed X-ray tomography and atomic force microscopy. Drawing is accompanied by crazing in the case of low-crystalline PLA, cracking in the case of annealed PLA, no defect in the case of plasticized PLA by physical blending, and shear bands and cracking in the case of plasticized PLA by reactive blending. These observations are discussed based on the initial structural features of the materials. © 2018 Wiley Periodicals, Inc. J. Polym. Sci., Part B: Polym. Phys. **2018**, *56*, 1452–1468

KEYWORDS: crazing; drawing; plasticization; polylactide; SAXS

INTRODUCTION In the case of petroleum-based thermoplastic polymers as poly(ethylene) (PE), poly(ethylene terephthalate) (PET), and poly(propylene) (PP), from the 1970s a great attention is focused on investigating their plastic deformation mechanisms to optimize their solid-state processing. Briefly, deformation mechanisms of such materials involve both chain orientation mechanisms, and the formation and growing of defects named deformation heterogeneities. In particular, deformation heterogeneities as cavitation by crazing and shear bands develop from the nanometer scale to the millimeter scale,[1–5] while chain orientation mechanisms induce phase transformation and lamella shearing.[6–8] All these aspects of plastic deformation are influenced by the polymer molecular weight, the polymer initial morphology, and the deformation temperature and strain rate.[3,8,9] Bio-based thermoplastic polymers are currently emerging to tentatively replace conventional petroleum-based ones due to environmental concerns. Among these bio-based polymers, polylactide (PLA) is one of the most attractive candidates because of its biodegradability and high tensile strength.[10] However, compared to petroleum-based polymers, PLA's deformation mechanisms were scarcely studied although this material is suitable for solid-state processing applications. In the pioneer works of Renouf-Glauser et al.,[11] deformation mechanisms of PLA were investigated upon drawing by time-resolved small-angle and wide-angle X-ray scattering (SAXS/WAXS) testing. At room temperature, PLA exhibited a limited plasticity that depended on the initial crystallinity. In particular, it was shown that PLA's elongation at break decreased with increasing crystallinity. In the case of amorphous PLA, deformation was dominated by deformation heterogeneities characterized by the formation and growing of crazes until the material failure, as shown by the progressive shifting of craze scattering peak to low scattering angles with increasing strain. In the case of semicrystalline PLA, deformation was controlled by chain orientation mechanisms engendering a progressive transformation of the lamella morphology into microfibrills.[11,12] Later, Stoclet et al.[13–16] reported new fundamental insights on the plastic deformation

mechanisms of amorphous and semicrystalline PLA. In the case of amorphous PLA, WAXS investigation showed that drawing above glass transition temperature (T_g) involved an orientation of amorphous chains leading to a mesomorphic phase and/or a strain-induced α′ crystalline phase, depending on the drawing temperature.[13,14] In the presence of an initial α crystalline phase, drawing above T_g engendered both the formation of α′ crystalline phase and mesomorphic phase, the proportion of each phase depending on the drawing temperature and initial crystallinity.[15] All these transformations were characterized by a lamellar to microfibrillar structural transformation, confirming previous works.[11] Last, below T_g, it was shown that the drawing of PLA involved both crazing and shear bands.[16] In particular, crazing only occurred at room temperature yielding no or a limited plasticity. With increasing temperature until 50 °C, plasticity increased due to the occurrence of shear bands. Novel crazes, called "shear band crazes," can be generated along shear bands, while conventional crazes formed after the occurrence of these shear band crazes. Therefore, bio-based thermoplastic polymers exhibited complex plastic deformation mechanisms characterized by a competition between chain orientation mechanisms, shear bands, and cavitation by crazing, depending on the temperature and the initial crystallinity.

To our best knowledge, deformation heterogeneities in PLA were not captured by a multiscale and *in situ* approach. For example, in the case of crazing, the dimensions of a craze can vary from the nanoscale to the millimeter scale in glassy polymers.[17] It was also shown that deformation heterogeneities in glassy polymers may involve first the formation of submicron crazes and then nanoscale crazes, highlighting the importance of conducting a multiscale investigation.[3] Crazing in PLA was only partially resolved, and hence, requires more representative and quantitative information.

The domination of crazing at room temperature during PLA drawing can be explained by a high chain rigidity combined with a high mass between entanglements.[18,19] To overcome this issue, PLA can be plasticized by mixing it with a miscible plasticizer. In this frame, we successfully conducted reactive extrusion of PLA with poly(ethylene glycol) methyl acrylate (acrylPEG) as plasticizer resulting in an improved elongation at break compared to the reference PLA at room temperature.[20] The obtained material, named pPLA, consisted in a plasticized PLA matrix with partially grafted and partially free inclusions of polymerized plasticizer. In addition, the plasticizer inclusions could bridge two PLA chains and a slightly crosslinked matrix was formed.[20,21] The chain orientation mechanisms of pPLA were quantitatively investigated in a previous paper by WAXS and differential scanning calorimetry (DSC),[22] but deformation heterogeneities were not studied despite an important whitening of the tensile specimens. Recently, an investigation was conducted to explain the whitening at the inclusion level of pPLA by combining (a) scanning transmission X-ray microscopy (STXM) coupled with near-edge X-ray absorption fine structure (NEXAFS) nanospectroscopy, and (b) microcomputed X-ray tomography (μCT).[23] It was qualitatively found that drawing caused a marked decrease of inclusion internal density without debonding with the matrix, and the formation of cracks bridging inclusions. However, deformation heterogeneities were not totally clarified in this previous paper.

This contribution aims at carefully identifying and analyzing deformation heterogeneities in PLA-based materials upon cold-drawing by a multiscale and *in situ* approach. The latter was based on the real-time identification and monitoring of deformation heterogeneities developing in the materials upon drawing. The millimeter scale was first examined by means of DIC applied to evaluate strain fields at the surface of tensile specimen. The micrometer scale was then studied by recording materials surface defects with an optical microscope during the drawing. Some complementary postmortem investigations of the defects induced by the deformation were done by μCT. Last, the nanometer scale was investigated by analyzing scattering objects with time-resolved SAXS at the synchrotron. Atomic force microscope (AFM) imaging of the material nanostructure was done at the postmortem state to complement SAXS measurements. The influence of the initial crystallinity on PLA's deformation heterogeneities was studied, as well as the influence of two plasticizing methods: reactive plasticization versus physical blending of PLA with acrylPEG.

EXPERIMENTAL

Materials and Processing

The PLA matrix of this study was the reference 4043D purchased from NatureWorks (Minnetonka, Minnesota). It was characterized by a D-isomeric unit content of 4.2%. As in previous works,[21,22] acrylPEG ($M_n \approx 480$ g mol^{-1}) from Sigma-Aldrich (Steinheim, Germany) was selected as a reactive plasticizer, while Luperox 101 (L101) from Sigma-Aldrich was used as a free-radical initiator. Prior to the extrusion, PLA pellets were dried at 50 °C overnight under vacuum. The reactive extrusion of PLA was conducted by means of a twin-screw mini-extruder Haake Rheomex OS PTW 16 manufactured by Thermo Scientific (Karlsruhe, Germany). This extruder was coupled with the motor Haake PolyLab OS drive from Thermo Scientific and had a screw diameter D of 16 mm. The barrel length L was configured to get the highest L/D ratio as possible, equal to 40 in this study that is believed to be suitable for reactive extrusion. Note that the processing conditions selected here yielded a residence time of about 5 min. The reactive extrusion procedure consisted of these successive stages: (a) 50 g of a PLA/acrylPEG/L101 mixture with compositions 79/20/1 in wt % were prepared and manually mixed in a beaker, (b) the mixture was then manually introduced in the first feed aperture of the extruder that was set to 200 °C in every zone, while screw speed was set to 100 rpm, (c) the obtained strands were cooled to room temperature in air and pelletized, (b) the pellets were introduced in a gravimetric micro twin screw feeder Brabender (Duisburg, Germany) set to a feeding rate of 20% (corresponding to about 1.3 kg h^{-1}), and (e) the pellets were finally extruded at 200 °C (in all

zones) at 100 rpm into films of thickness comprised between 0.2 and 0.3 mm by means of a sheet die coupled with a contact roller positioned onto a conveyor belt. In the case of PLA and the simple mixing between PLA and acrylPEG, only one extrusion step was conducted. The following formulations of PLA/acrylPEG/L101 were prepared (composition in wt %): 100/0/0 (PLA), 80/20/0 (PLA/acrylPEG), and 79/20/1 (pPLA). For the annealing procedure, the PLA film samples were heated between two metal plates at 100 °C for 2 h in an oven (Thermo Scientific Heraeus, Waltham, Massachusetts) under vacuum. After 2 h, the heating was stopped and the samples were slowly cooled to room temperature under vacuum. The resulting samples were called aPLA (PLA after annealing).

Differential Scanning Calorimetry

The thermal properties of the PLA-based materials were measured by DSC with a Netzsch DSC 204 F1 (Selb, Germany). To this end, samples with a mass comprised between 3 and 5 mg were cut from the films and subjected first to a cooling stage from room temperature to −100 °C at a rate of −10 °C min^{-1} then, samples were heated to 180 °C with a rate of 10 °C min^{-1}. The glass transition temperature (T_g), the cold crystallization temperature (T_{cc}), the cold crystallization enthalpy (ΔH_{cc}), the melting temperature (T_m), and the melting enthalpy (ΔH_m) of the samples were obtained from this heating stage to get the properties of the as-processed materials. The crystallinity was calculated based on eq 1 where x_{PLA} was the total weight fraction of PLA (0.79 in pPLA, 0.80 in PLA/acrylPEG, and 1.00 in PLA), and $\Delta H_{m,0}$ was the melting enthalpy of a 100% crystalline PLA determined to be $\Delta H_{m,0}$ = 93 J g^{-1}:[24]

$$X_c = \frac{\Delta H_m - \Delta H_{cc}}{x_{PLA} \times \Delta H_{m,0}} \quad (1)$$

Tensile Testing

A miniature tensile/compression module Kammrath & Weiss (Dortmund, Germany) was used to draw PLA-based materials while submitted at the same time to *in situ* measurements. This machine was equipped with a 5 kN load cell (1 N of resolution within all the load range), and a linear variable differential transformer enabling to measure sample elongation. Dumbbell tensile specimens with an overall length of 50 mm and a grip section width of 10 mm were carefully cut from the extruded film with their axis oriented parallel to the extrusion direction. As main characteristics, tensile specimen had a grip section length of 15 mm, a length of reduced parallel section of 20 mm, and a minimum width W_0 of 5 mm. The specimens were drawn with an initial stroke length L_0 of about 18.7 mm, at a temperature of 20 °C, and with a crosshead displacement speed $\Delta L/\Delta t$ of 10 μm s^{-1}. The engineering strain ε_{eng} (in %), defined along the Axis 1 as represented in Figure 1, was calculated as $100 \times (\Delta L/L_0)$ and the corresponding strain rate $\Delta\varepsilon_{eng}/\Delta t = 1/L_0 \times \Delta L/\Delta t$ was evaluated to be 2.7×10^{-4} s^{-1}. The engineering stress σ_{eng} was calculated from the measured load divided by the initial cross-section S_0. The tensile measurements were conducted *in situ* using three different techniques to obtain a multiscale analysis of the deformation heterogeneities: (a) DIC at the millimeter scale, (b) optical microscope at the micrometer scale, and (c) time-resolved SAXS at the nanometer scale. It is important to note that these three *in situ* techniques were not operated at the same time, but successively.

Time-Resolved SAXS

Time-resolved SAXS experiments were carried out at the Austrian SAXS beamline of the Elettra synchrotron (Trieste, Italy) with a photon energy of 8 keV that corresponded to the Cu k_α wavelength radiation of 0.154 nm. The incident X-ray beam hitting the specimen had the dimensions of about 2000 × 250 μm (rectangle with its major axis parallel to the tensile direction). The scattering signal was recorded by means of a 2D detector Pilatus 100 K from Dectris (Baden, Switzerland), using an acquisition time of 20 s. The detector was positioned at about 1.80 m from the samples, which allowed to measure periodicities ranging from 4 to 60 nm.

Here below is detailed the data reduction procedure of the SAXS patterns that can be initially represented as $I_{exp}(pixel_1, pixel_2)$ where I_{exp} was the experimental intensity of each pixel in the (1,2) axis system (Fig. 1). The objective of the data reduction procedure was to extract information about deformation heterogeneities in PLA-based materials upon drawing.

i. Before the measurement, a background image was recorded $I_{bkg}(pixel_1, pixel_2)$ without specimen and then it was subtracted from all images $I_{exp}(pixel_1, pixel_2)$ by means of the software ImageJ (National Institutes of Health). The resulting background-corrected images were named $I_{cor}(pixel_1, pixel_2)$. A typical background-corrected $I_{cor}(pixel_1, pixel_2)$ image was represented in Figure 1(a) in the case of PLA drawn at 20 °C at an engineering strain ε_{eng} of 4% and with a strain rate of 2.7×10^{-4} s^{-1}. Crazing scattering was characterized by a meridian scattering engendered by the reflection of the craze surfaces (or walls) and by an equatorial scattering engendered by the craze fibrils, as previously described.[16,25]
ii. The scattering vector q-calibration of background-corrected images was done with a silver behenate sample supplied by the synchrotron SAXS beamline laboratory. The calibration parameters (beam center, detector distance, tilt plane rotation angle, tilt angle, and proportional D-spacing) were determined by means of the software Fit2D (European Synchrotron Radiation Facility, Grenoble, France) and used to transform the $I_{cor}(pixel_1, pixel_2)$ images into $I(q, \phi)$ images in which the scattering intensity I depends now on the scattering vector q, and the azimuthal angle ϕ.
iii. Inspired by a previous methodology,[25] two regions were considered on the $I(q, \phi)$ images as represented in Figure 1(b). The first region, called equatorial region, was dominated by craze fibrils scattering intensity $I_{eq}(q)$, and the second region, called meridian region, was dominated by the craze surfaces scattering intensity $I_{me}(q)$. The

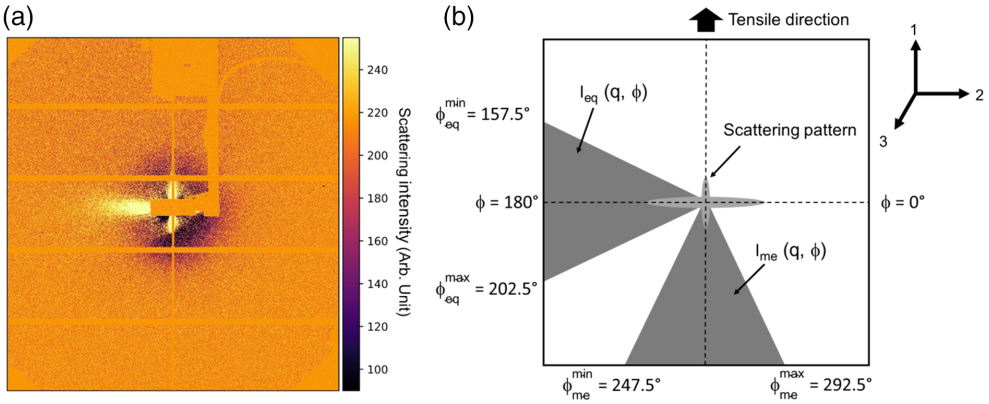

FIGURE 1 (a) Typical background-corrected scattering pattern of PLA drawn at 20 °C at 2.7×10^{-4} s^{-1} at an engineering strain of 4%, and (b) principle of azimuthal intensity integration in the equatorial and meridian regions showing scattering by craze fibrils and craze surfaces, respectively. [Color figure can be viewed at wileyonlinelibrary.com]

azimuthal integration of the scattering intensities $I_{me}(q)$ and $I_{eq}(q)$ was calculated with the software Fit2D as follows:

$$I_{me}(q) = \int_{q_{me}^{min}}^{q_{me}^{max}} I_{me}(q,\phi)\mathrm{d}\phi \tag{2}$$

$$I_{eq}(q) = \int_{q_{eq}^{min}}^{q_{eq}^{max}} I_{eq}(q,\phi)\mathrm{d}\phi \tag{3}$$

where $I_{me}(q, \phi)$ was the scattering intensity in the meridian region from q_{me}^{min} = 157.5° and q_{me}^{max} = 202.5°, and $I_{eq}(q, \phi)$ was the scattering intensity in the equatorial region from q_{eq}^{min} = 247.5° and q_{eq}^{max} = 292.5°, as represented in Figure 1(b). In the two cases, an azimuthal range of 45° was considered for the intensity integration that included all the scattering intensity from the craze surfaces and from the craze fibrils.

iv. The 1D scattering intensity profiles $I_{me}(q)$ and $I_{eq}(q)$ were corrected from the sample thickness absorption based on the following equations:

$$I_{me}^{c}(q) = I_{me}(q)\exp\left(\frac{\mathrm{k}t_s}{\cos(2\theta)}\right) \tag{4}$$

$$I_{eq}^{c}(q) = I_{eq}(q)\exp\left(\frac{\mathrm{k}t_s}{\cos(2\theta)}\right) \tag{5}$$

where θ was the scattering angle, k was the absorption coefficient of PLA taken to be 9.23 cm^{-1}, t_s was the specimen thickness, $I_{me}^{c}(q)$ was the absorption-corrected scattering intensity in the meridian region, and $I_{eq}^{c}(q)$ was the absorption-corrected scattering intensity in the equatorial region. As detailed in the section "Digital Image Correlation," specific cameras were used to extract strain field on the tensile specimen main face upon drawing, but not during time-resolved SAXS measurements. The specimen thickness reduction along Axis 3 (Fig. 1) was not monitored, but the two transversal strains ε_{22} and ε_{33} were supposed to be similar enabling to calculate t_s:

$$t_s = t_s^0 \exp\varepsilon_{22} \tag{6}$$

where t_s^0 was the initial specimen thickness measured with a micrometer.

v. $I_{me}^{c}(q)$ and $I_{eq}^{c}(q)$ were integrated in the investigated q range using the following equations:

$$I_{me}^{c} = \int_{q_{me}^{min}}^{q_{me}^{max}} I_{me}^{c}(q)\mathrm{d}q \tag{7}$$

$$I_{eq}^{c} = \int_{q_{eq}^{min}}^{q_{eq}^{max}} I_{eq}^{c}(q)\mathrm{d}q \tag{8}$$

where q_{me}^{max} = 2.12 nm^{-1}, q_{me}^{min} = 2.44×10^{-1} nm^{-1}, q_{eq}^{max} = 2.31 nm^{-1}, and q_{eq}^{min} = 9.86×10^{-2} nm^{-1}.

vi. The volume of the scatterers related to the true invariants Q_{me}^{t} and Q_{eq}^{t} was expressed as follows:[26]

$$Q_{me}^{t} = V^{-1}\int_0^{\infty} I_{me}^{c}(q)\mathrm{d}q \tag{9}$$

$$Q_{eq}^{t} = V^{-1}\int_0^{\infty} I_{eq}^{c}(q)\mathrm{d}q \tag{10}$$

where V was the irradiated specimen volume. In the case of craze fibrils scattering, Q_{eq}^{t} could enable to calculate the fibril radius that was, for example, comprised between 3 and 7 nm in the case of high impact polystyrene upon drawing at room temperature, depending on the used model.[27] Furthermore, Q_{me}^{t} could enable to determine quantitative information about craze dimensions and volume fraction, based, for example, on a disk shape model.[3] In our case, the true invariants could not

be determined because their calculations required data in all q angle range, and because the scattering intensity was not calibrated in absolute unit. For simplification, effective invariants Q^{e}_{me} and Q^{e}_{eq} in the investigated q range were calculated based on:

$$Q^{e}_{me} = V^{-1}\int_{q^{min}_{me}}^{q^{max}_{me}} I^{c}_{me}(q)dq = I^{c}_{me}/V \quad (11)$$

$$Q^{e}_{eq} = V^{-1}\int_{q^{min}_{eq}}^{q^{max}_{eq}} I^{c}_{eq}(q)dq = I^{c}_{eq}/V \quad (12)$$

Upon drawing, V can be calculated based on the irradiated surface (2000 μm × 250 μm) multiplied by the specimen thickness t_s taken in nm:

$$V = 5\times10^{11}t_s \quad (13)$$

vii. To eliminate a possible effect of lamella scattering for each deformation step, the initial invariant values Q^{o}_{me} and Q^{o}_{eq} were systematically subtracted to Q^{e}_{me} and Q^{e}_{eq} as follows:

$$Q_{me} = Q^{e}_{me} - Q^{o}_{me} \quad (14)$$

$$Q_{eq} = Q^{e}_{eq} - Q^{o}_{eq} \quad (15)$$

For simplification, we basically considered here that Q_{me} was proportional to the volume fraction of the craze surfaces,[2,3,26,28] and that Q_{eq} was proportional to the volume fraction of the craze fibrils.

Digital Image Correlation

The DIC was conducted with an Aramis 6 M system from Gom Optical Measuring Techniques (Braunschweig, Germany). The system was equipped with two cameras to allow a 3D analysis of the material strain field. The samples were first painted with white color and afterward speckled with a spray of black color creating a pattern that allowed the DIC process by the software Aramis Professional. The images were recorded with a constant frame rate of 1 Hz during the tensile testing with the miniature tensile machine described above. Only the main tensile specimen face was visualized for the DIC procedure. To obtain the axial and transversal strains of the samples, two gauges called Point distances in the software were created in the center of the specimen with an initial gauge length of about 1.5 mm. Based on the measured axial distance $l_{t,\ axial}$ and transversal distance $l_{t,\ transversal}$ at a given time, and the corresponding initial distances ($l_{0,\ axial}$ and $l_{0,\ transversal}$), the axial (ε_{11}) and transversal (ε_{22}) strains were calculated with the eqs 16 and 17, respectively.

$$\varepsilon_{11} = \ln\left(\frac{l_{t,axial}}{l_{0,axial}}\right) \quad (16)$$

$$\varepsilon_{22} = \ln\left(\frac{l_{t,transversal}}{l_{0,transversal}}\right) \quad (17)$$

Due to the low thickness of the samples, the second transversal strain (ε_{33}) was not measured, but it was assumed that $\varepsilon_{33} \approx \varepsilon_{22}$. A rough estimation of the volume strain (ε_v) can be obtained as the sum of the strains in the three directions,[29] as described by eq. 18:

$$\varepsilon_v = \varepsilon_{11} + \varepsilon_{22} + \varepsilon_{33} = \varepsilon_{11} + 2\varepsilon_{22} \quad (18)$$

In the case where deformation heterogeneities are crazes, an increase of volume strain is expected.[4] The true stress σ_{11} was calculated by eqs 19 and 20, where F was the load in N measured with the miniature tensile machine, and S_0 in mm^2 was the initial cross-section of the specimen. Note that the variation of the specimen cross-section was taken into account with the aforementioned assumption that the two transversal strains are equal.

$$\sigma_{11} = \frac{F}{S_0}\exp(-(\varepsilon_{22}+\varepsilon_{33})) \quad (19)$$

$$\sigma_{11} = \frac{F}{S_0}\exp(-2\varepsilon_{22}) \quad (20)$$

Micro-Computed X-Ray Tomography

Some complementary μCT imaging of the deformation heterogeneities developing in PLA plasticized by reactive extrusion was conducted at the postmortem state. The utilized equipment was a 3D X-ray microscope reference Xradia 510 from Zeiss (Pleasanton, California) enabling a spatial resolution of about 1 μm whatever the sample position relative to the X-ray source. The drawn sample of plasticized PLA was cut along the minimum section and one half was positioned on the sample holder for the analysis. One highly deformed region appearing white was investigated, and compared with a nondeformed specimen. The image acquisition was done with a 20× objective during 20.3 h at 40 kV, and 3 W. The region was reconstructed in 3D with a voxel size of 0.3 μm.

Optical Microscopy

To observe deformation heterogeneities of the samples under optical probing, the miniature tensile machine was positioned on the sample stage of a stereomicroscope Leica MZ 125 (Heerbrugg, Switzerland) with a ×20 objective. The central section of the samples was observed during the tension and images were recorded. For PLA and aPLA, one image per second was recorded, while for pPLA and PLA/acrylPEG, one image each 5 s was recorded due to the higher ductility of plasticized PLA compared to neat PLA and aPLA. The recorded images were treated and analyzed by means of the software ImageJ (National Institutes of Health, Bethesda, Maryland). To this end, the images were first converted to black and white images by a gray-level thresholding enabling to isolate the defects from the rest of the image. Then, the surface density of the defects S_d/S, where S_d was the surface occupied by the defects and S was the image surface, was calculated by the software.

Scanning Transmission X-Ray Microscopy

The complex microstructure of pPLA was imaged by STXM equipped with NEXAFS nanospectroscopy. By means of this

TABLE 1 Initial Properties of the As-Processed Materials in Terms of Crystallinity (X_c) and Glass Transition Temperature (T_g) Determined from DSC Measurement, Matrix and Inclusion Elastic Modulus Determined by AFM, and Presence of Crosslinking and Grafting (With Standard Deviation in BRACKETS)

Material	Processing	X_c (%)	T_g (°C)	Grafting and Crosslinking	Elastic Modulus of the Matrix (GPa)[a]	Elastic Modulus of the Inclusion (GPa)[a]
PLA	Extrusion	4.6 (1.2)	62.5 (0.2)	No	2.40 (0.26)	–
aPLA	Extrusion and annealing	28.1 (0.9)	63.9 (0.4)	No	[b]	–
pPLA	Plasticization by reactive extrusion	13.5 (0.5)	36.4 (0.6)	Yes	2.60 (0.26)	0.23 (0.04)
PLA/acrylPEG	Plasticization by extrusion	14.5 (1.3)	11.4 (1.6)	No	1.79 (0.10)	0.04 (0.01)

[a] From Ref. [23]

[b] Not measured.

technique, it was possible to distinguish the different polymeric phases of pPLA, and hence, the plasticizer inclusions were clearly observed. Such analyses were conducted at the PolLux beamline of the Swiss Light Source synchrotron (Paul Scherrer Institute, Villigen, Switzerland) based on a previous protocol.[23] The composition mapping of PLA (resonance at 288.5 eV) and acrylPEG (289.7 eV) were represented.

Atomic Force Microscopy

AFM imaging of drawn samples of PLA, aPLA, and pPLA was conducted with an Asylum MFP 3D Infinity (Santa Clara, California) at the postmortem state. The samples were all deformed with the miniature tensile/compression module described above. Topography and frequency images were recorded at 1 Hz by means of the bimodal tapping measurements carried out in an amplitude modulation–frequency modulation (AMFM) mode. To this end, the utilized tips were the model number AC 160 R3 from Asylum research, whose resonance frequency and force constant were approximately 300 kHz and 26 N m^{-1}, respectively. The samples of PLA, aPLA, and pPLA were directly observed without any particular preparation.

RESULTS AND DISCUSSION

Initial Properties

Before analyzing deformation heterogeneities, it is important to describe the main characteristics of the PLA-based materials that are summarized in Table 1. Here are reported for each material (a) the processing description, (b) the crystallinity X_c and glass transition temperature T_g measured by DSC, (c) the presence or not of grafting and crosslinking, and (d) the elastic modulus of the matrix and inclusions assessed by AFM in a previous study.[23] The knowledge of material properties may enable to do hypotheses on their possible deformation heterogeneities.

PLA referred to the unmodified reference samples of PLA films having a low crystallinity (X_c = 4.6 wt %). To increase the initial crystallinity, the films of PLA were annealed at 100 °C, the resulting samples being named aPLA. The initial crystallinity increased from 4.6 wt % for PLA to 28.1 wt % for aPLA. At the same time, the glass transition temperature (T_g) slightly increased from 62.5 °C in the case of PLA to 63.9 °C in the case of aPLA, as a direct effect of the crystallinity increase that may confine amorphous chain segmental motions to achieve the glass transition. The increase of crystallinity between PLA and aPLA should be accompanied by an increase of the matrix elastic modulus but that of aPLA was not previously measured.[23] Matrix elastic modulus of aPLA can be related to the Young's modulus of the material that increased from 2.9 GPa in the case of PLA to 3.5 GPa in the case of aPLA (the tensile behavior of the materials is briefly discussed in the next section of the paper). Based on the literature, crazing is identified as deformation heterogeneity in PLA below its T_g,[16] because of its high intrinsic chain rigidity and high mass between entanglements.[18,19] So, it is hypothesized that the multiplication of rigid lamellae due to annealing may only influence craze propagation. In particular, the presence of lamellae may hinder craze propagation engendering a coalescence of the crazes and a faster breaking of the material compared to amorphous PLA.

The microstructure of pPLA observed by STXM/NEXAFS is represented in Figure 2. In particular, PLA-rich domains corresponding to the matrix [Fig. 2(a)], and acrylPEG-rich domains corresponding to the inclusions [Fig. 2(b)] were noted. These inclusions had a quite broad size distribution ranging from the sub-micron scale to the micron scale. Inside the inclusions, the distribution of the acrylPEG-rich domains appeared heterogeneous, which was previously discussed,[23] as well as the overall chemical reactions occurring during the reactive extrusion.[24,30] The presence of crosslinkings in pPLA is qualitatively proved by the formation of an instable gel when pPLA is immersed in chloroform or tetrahydrofuran, while PLA is totally soluble in these two solvents [Fig. 2(c)]. Unfortunately, the gel of pPLA being unstable, their analyzing to determine a crosslinking density was not relevant. Concerning the grafting of the plasticizer onto PLA, it was proved by the partial extraction of poly(acrylPEG) from pPLA during soxhlet extraction procedure in methanol.[20,21] As a comparison to the reactive extrusion, the physical blending of PLA with acrylPEG

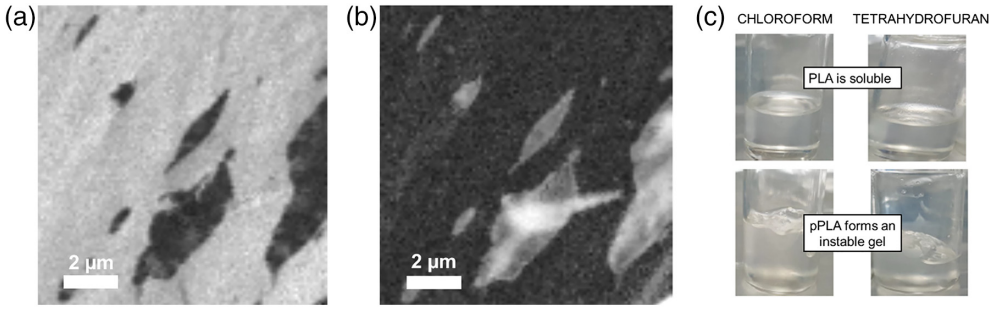

FIGURE 2 (a) PLA composition image recorded at 288.5 eV and (b) poly(acrylPEG) composition image recorded at 289.7 eV obtained from STXM measurements in the case of as-processed pPLA, (c) solubility of as-processed PLA and pPLA in chloroform and tetrahydrofuran. [Color figure can be viewed at wileyonlinelibrary.com]

was also done. The resulting samples referred to PLA/acrylPEG. In this case, neither grafting nor crosslinking was obviously observed. Both plasticization methods increased the crystallinity in comparison to PLA from 4.6 to 13.5 wt % for pPLA and from 4.6 to 14.5 wt % for PLA/acrylPEG. Therefore, the plasticizing facilitates the crystallization of PLA probably due to an increased chain mobility. As described in previous works,[21,23] the reactive plasticization decreased the glass transition temperature of PLA from 62.5 to 36.4 °C in the case of pPLA. Concerning PLA/acrylPEG, just a frail glass transition was visible at 11.4 °C indicating a more important decrease of T_g compared to pPLA. It was argued that the very low glass transition temperature of PLA/acrylPEG was due to the dispersion of low-molecular-weight acrylPEG plasticizer within PLA matrix. Indeed, this process drastically increases PLA free volume, and hence reduces PLA chain physical interactions resulting in higher segmental motions.[21] In the case of pPLA, a partial replacement of the highly plasticized PLA with high-molecular-weight poly(acrylPEG) dispersed within the matrix and grafted onto it occurs. Therefore, the dispersion state of the plasticizer and consequently the efficiency of the plasticizing in pPLA are supposed to be reduced compared to the blend PLA/acrylPEG. The local elastic modulus measurements showed that the elastic modulus of the matrix increased from 2.4 GPa for PLA to 2.6 GPa in the case of pPLA, and on the contrary the elastic modulus of the matrix decreased from 2.4 GPa for PLA to 1.79 GPa in the case of PLA/acrylPEG. The inclusions in pPLA had an elastic modulus of 0.23 GPa, while those in PLA/acrylPEG had a modulus of 0.04 GPa. It was explained that the increased matrix elastic modulus from PLA/acrylPEG to pPLA resulted from the presence of graftings and crosslinkings. At the same time, reactive extrusion engenders a polymerization of acrylPEG explaining the increase of inclusion elastic modulus from PLA/acrylPEG to pPLA.[23] Compared to PLA, the significant decrease of T_g and the decrease in matrix rigidity of PLA/acrylPEG can enhance chain orientation mechanisms limiting deformation heterogeneities. It is also thought that the presence of plasticizer inclusions in PLA/acrylPEG with a very low elastic modulus does not play any significant rule on the deformation heterogeneities. The complex structure of pPLA makes hypotheses about deformation heterogeneities quite complicated. In comparison with PLA/acrylPEG, the higher matrix elastic modulus and T_g of pPLA can contribute to limit chain amorphous orientation, and hence, can enhance deformation heterogeneities. The presence of polymerized acrylPEG inclusions can also play a role on these deformation heterogeneities that has to be determined.

Mechanical Behavior

PLA, aPLA, pPLA, and PLA/acrylPEG were drawn in tension with the miniature tensile machine at 2.7×10^{-4} s^{-1} and 20 °C. It is important to note that due to the displacement limit of the machine, it was not possible to draw sample more than an engineering strain ε_{eng} of 15%. At the same time, DIC enabled to determine the true stress σ_{11} versus true strain ε_{11} curves of the materials that are represented in Figure 3(a). It can be seen that aPLA reached a very low axial strain at break (ε_{11} = 0.08), while on the contrary pPLA reached a much higher axial strain without breaking (ε_{11} = 0.71 at the maximum tensile machine displacement).

PLA had a Young's modulus of 2.9 GPa, which is in good accordance with the literature.[31] The yield point was reached at ε_{11} = 0.02 and corresponded to a stress of 38.8 MPa, a value slightly higher than the breaking stress found to be of 36.0 MPa. PLA broke under the chosen experimental conditions in the ductile region at a true strain ε_{11} of 0.18, corresponding to about four times the engineering strain at the rupture of about 4%. This finding clearly indicates a localization of strain at the center of tensile specimen.

Concerning the true stress-true strain curve of aPLA [Fig. 3 (a)], it exhibited marked differences compared to that of PLA. The Young's modulus of aPLA was about 3.5 GPa, which was 21% higher than for PLA (2.9 GPa) and can be related to the higher initial crystallinity.[11] The yield point occurred for both samples at a strain of about 0.02. While the engineering stress–strain measurements obtained similar elongation at break values for PLA and aPLA, the true strain at break for PLA (ε_{11} = 0.18) was about two times higher than for aPLA (ε_{11} = 0.08), although the engineering strain at break is about 4% for PLA and aPLA. These different true axial strains at break values can be reasoned by an increased strain

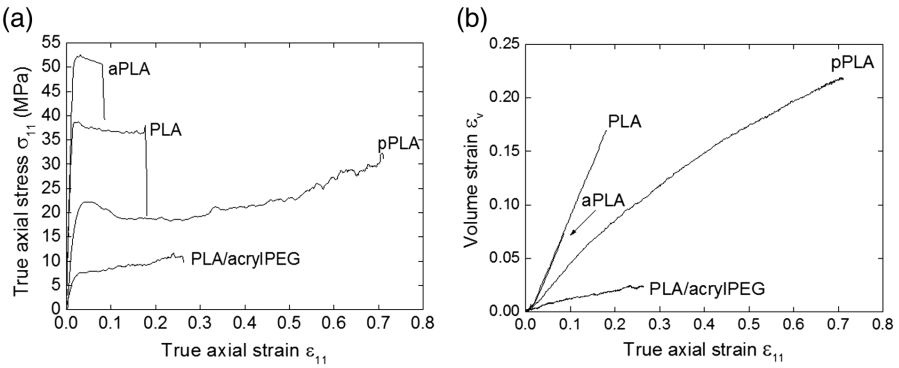

FIGURE 3 True axial stress versus true axial strain of the materials drawn at 20 °C and 2.7×10^{-4} s^{-1}, pPLA and PLA/acrylPEG did not break at the maximum displacement of the miniature tensile machine.

localization induced by the annealing, as it was observed for annealed polystyrene.[32]

As already mentioned, the tensile deformation of the two plasticized PLA samples pPLA and PLA/acrylPEG reached the limits of the testing equipment (maximum engineering strain of 15%) and therefore their elongations were much higher compared to the two nonplasticized PLA materials ($\varepsilon_{eng} \approx 4\%$). The two plasticization methods lead to different tensile behaviors as it can be observed in Figure 3(a). While PLA and aPLA had a Young's modulus of 2.9 and 3.5 GPa, respectively, pPLA and PLA/acrylPEG exhibited lower values equal to 1.1 and 0.4 GPa, respectively. These lower Young's moduli indicate a decrease in stiffness for both plasticized samples compared to the PLA samples, but the reactive extrusion with a free-radical initiator supports the toughness-ductility balance and allows to keep a moderate tensile modulus.[33] It is well known, that blending of PLA with acrylPEG leads to a rubber-like material with low stress values and a low initial tensile modulus.[21,30] The decrease in stiffness was also reflected by the lower stress values that were obtained by the plasticized samples. The pPLA sample with graftings and crosslinkings showed a clear yield point with a stress level of 21.9 MPa and then a strain softening reducing stress to 19.0 MPa, followed by a strain hardening region up to 29.8 MPa. The pPLA material behaved like PLA at temperatures close to their glass transition temperature.[34,35] In contrast, PLA/acrylPEG offered lower stress levels for the whole testing with a yield stress of 7.3 MPa, and no strain softening but a continuous strain hardening reaching a final stress of 10.6 MPa.

The evolution of ε_v as a function of axial strain ε_{11} is plotted in Figure 3(b) for all the materials. Obviously, ε_v determined from strains taken at the specimen surface and with the transverse isotropy hypothesis ($\varepsilon_{22} \approx \varepsilon_{33}$) cannot rigorously be associated with the volume strain of the materials. The measurement of ε_v can be considered as indicating the tendency to dilatation of a polymer. Accordingly, the dilatation tendency increased in this material order: PLA/acrylPEG < pPLA < aPLA ≈ PLA. Dilatation can be engendered by the deformation heterogeneities and in particular by crazing or cracking. As it can be seen, the measurement of ε_v could not distinguish between PLA and aPLA, but the true strain at break is lower in aPLA compared to PLA probably indicating different deformation heterogeneities. The low volume strain of PLA/acrylPEG compared to PLA also confirmed our hypothesis on the fact that deformation heterogeneities may be limited in PLA/acrylPEG compared to PLA. The higher dilatation ability of pPLA compared to PLA/acrylPEG may reflect more deformation heterogeneities by cavitation in pPLA compared to PLA/acrylPEG. Further investigations are obviously needed to verify all these hypotheses.

Some true axial strain field measurements are provided in Figure 4 for the four materials, based on DIC analysis. In particular, the strain fields were determined at an engineering strain of about 4% for PLA [Fig. 4(a)] and aPLA [Fig. 4(b)], at an engineering strain of about 15% for PLA/acrylPEG [Fig. 4(c)], and pPLA [Fig. 4(d)]. Such measurements provided information about the localization of strain in the center of tensile specimen, associated with necking. Although PLA and aPLA have the same engineering strain of about 4%, the strain at the center of PLA specimen is higher than in the case of aPLA, indicating a higher strain localization in PLA. Furthermore, the strain localization on PLA specimen appeared to follow diagonal lines, this phenomenon being also present but less marked in aPLA. Furthermore, in the case of PLA and aPLA, strain appeared to be more important at the specimen edges compared to the specimen center [Fig. 4(a,b)]. When comparing PLA/acrylPEG with pPLA at the same engineering strain of about 15%, pPLA exhibited a more important axial strain at the center of tensile specimen compared to PLA/acrylPEG, and hence, a higher strain localization.

Some pictures of the tensile specimen are provided in Figure 5. In the case of PLA and aPLA after the breaking of the specimen, some defects were noted in the central region of the specimen [Fig. 5(a,b)]. These defects appeared as parallel lines oriented at $\pm 80°$ to 85° to the drawing direction in the case of PLA, and crossing lines oriented at $\pm 80°$ to 85 ° to the drawing direction in the case of aPLA. Furthermore, the defect lines seemed thinner in PLA compared to aPLA. Such defects correlate with the strain field observations showing diagonal areas of strain localization [Fig. 4(a,b)]. In the case of PLA/acrylPEG, no defect was noted on the specimen picture

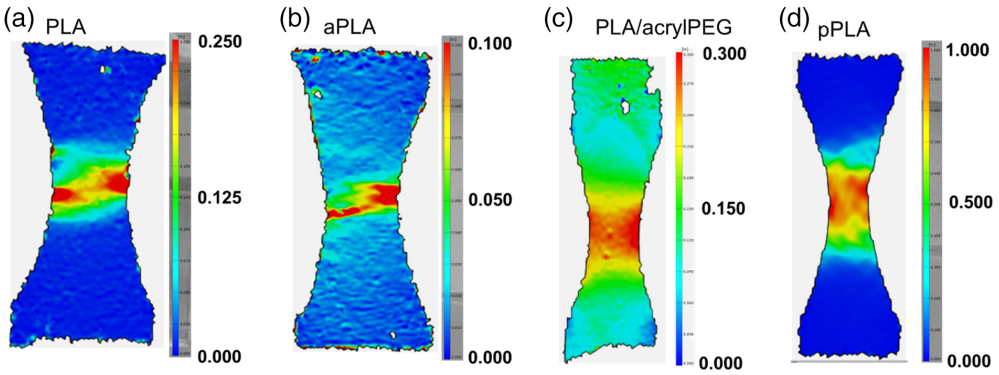

FIGURE 4 *In situ* DIC assessment of true strain field during the tensile testing of (a) PLA at $\varepsilon_{eng} \approx 4\%$, (b) aPLA at $\varepsilon_{eng} \approx 4\%$, (c) pPLA at $\varepsilon_{eng} \approx 15\%$, and (d) PLA/acrylPEG at $\varepsilon_{eng} \approx 15\%$. [Color figure can be viewed at wileyonlinelibrary.com]

[Fig. 5(c)]. Last, concerning pPLA, an important density of defects covering almost all the gauge section of the tensile specimen was observed [Fig. 5(d)]. The density of these defects was maximum at the center of the specimen. These defects seemed to be crossing lines with an orientation of $\pm 5°$ to 10 ° compared to the tensile direction.

In semicrystalline polymers, the occurrence of necking, and hence, strain localization is a complex phenomenon starting when the yield point is reached. At this point, some local structural reorganizations engender a strain localization, as for example, the onset of crystal unfolding.[36] In the case of glassy amorphous polymers, the onset of plastic deformation when the yield point is reached engenders a change of the local molecular packing resulting in a strain-softening phenomenon, as noted in Figure 3(a). As a consequence, strain localization occurs and manifests as necking.[37] Generally, strain localization is noted at the center of a tensile specimen, but in the case of glassy amorphous polymers, the presence of specimen edge defects induced by the cutting locally promote plastic deformation and can explain why strain localization on PLA and aPLA specimen follows diagonal lines [Fig. 4(a,b)]. At the onset of plasticity, deformation of semicrystalline polymers is generally ascribed to a competition between chain orientation mechanisms and deformation heterogeneities. In PLA, it has been reported that deformation heterogeneities as crazing and shear bands are prominent below T_g due to the high chain rigidity and/or the high mass between entanglements that limit chain orientation mechanisms.[16,18,19] In particular, at room temperature, crazing was proved to be the unique deformation heterogeneity in PLA upon drawing, while both shear bands and crazing were noted at 50 °C.[16] Shear bands were characterized by very straight crossing lines along slip planes roughly oriented at $\pm 45°$ to the drawing direction.[16] This implies that in PLA the defect lines are probably crazes (no shear band at room temperature), while in aPLA and pPLA the defects appearing as crossing lines at $\pm 80°$ to 85° to drawing direction could be crazes and/or specific shear

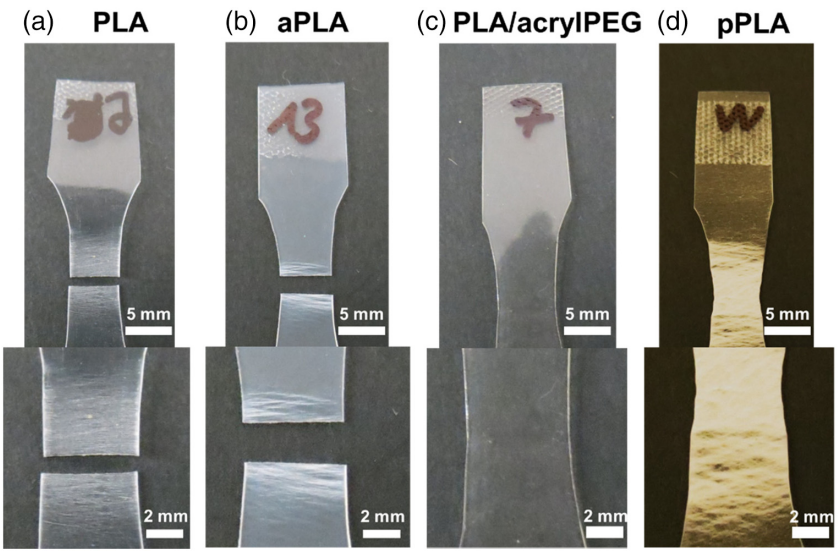

FIGURE 5 Pictures of (a) PLA sample drawn until breaking, (b) aPLA sample drawn until breaking, (c) PLA/acrylPEG sample drawn until $\varepsilon_{eng} \approx 15\%$ and unloaded, and (d) pPLA sample drawn until $\varepsilon_{eng} \approx 15\%$ and unloaded. [Color figure can be viewed at wileyonlinelibrary.com]

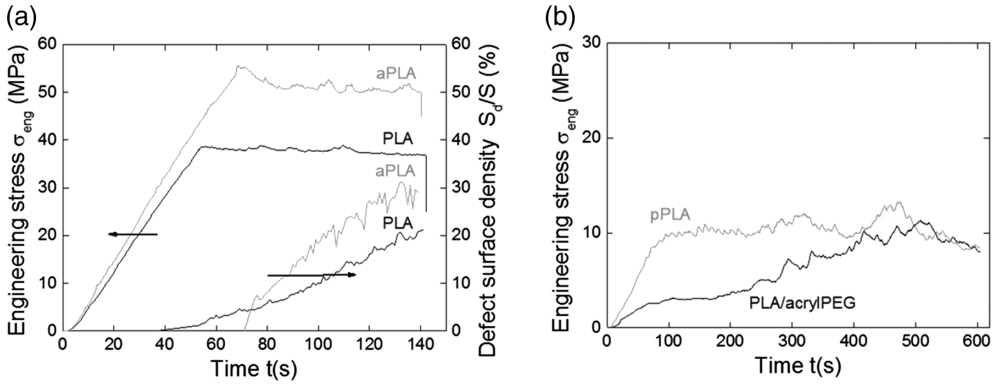

FIGURE 6 Engineering stress versus time curves in the case of (a) PLA and aPLA, and in the case of (b) PLA/acrylPEG and pPLA, when drawn at 20 °C and 2.7×10^{-4} s^{-1}. For PLA and aPLA, the evolution of defect surface density with time was also plotted.

bands since their characteristics do not reflect the ones of conventional shear bands. A detailed identification of deformation heterogeneities developing in PLA, aPLA, and pPLA upon drawing is now required, by investigating them at the microscale and nanoscale.

Microscale Analysis of Deformation Heterogeneities

Deformation heterogeneities in PLA-based materials were investigated in real-time by an optical microscope monitoring during the tensile testing. The engineering stress versus time curves of the materials drawn at 20 °C and 2.7×10^{-4} s^{-1} are plotted in Figure 6(a,b), while some relevant pictures of the materials are shown in Figure 7, and the extracted surface density of the defects S_d/S is represented in Figure 6(a).

In the case of PLA, the formation of defects was noted at around 45 s (strain of 1.3%) just before the yield point [Fig. 7(a)]. Such defects were parallel lines oriented at ±85° to the drawing direction axis, confirming previous observations [Figs. 4(a) and 5(a)]. Then, the surface density of the defects progressively increased reaching a maximum of 21.2% at the specimen rupture [Fig. 7(b,c)]. In the case of aPLA, defects were detected at the yield stress [about 70 s, Figs. 6(a) and 7(d)] and appeared as crossing lines oriented at ±85° to the drawing direction. Their surface density rapidly increased until 29% at the specimen rupture [Figs. 7(e)–(f)], which was higher than for PLA. Another difference compared to PLA was that the slope of S_d/S versus time that was more important in the case of aPLA indicating a faster defect growing. Furthermore, it appeared that the defects developing in aPLA were less linear, and hence, more tortuous in comparison with PLA [Fig. 7(b,e)]. In Figure 7(f), some coalescence of defects were also noted in the case of aPLA. It is to be noted that for PLA and aPLA, only one size population of defects was noted. Concerning plasticized PLAs, PLA/acrylPEG did not exhibit any defect during its drawing [Figs. 7(g–i)], while pPLA exhibited the formation of very small defects from about 84 s corresponding to the yield point [Fig. 7(j–l)]. These defects are oriented perpendicular to tensile direction and could be crazes or cracks. Based on Figure 7(k), such defects were connected or not to inclusions. An accurate quantification of these defects by image analysis was not possible since in many areas it was not possible to distinguish between the defects and the matrix. The next step of this work is an analysis of deformation heterogeneities developing in PLA-based materials at the nanoscale by time-resolved SAXS. Indeed, it will be possible to distinguish between crazes, shear bands, and cracks, since shear bands do not scatter X-ray, crazes exhibited a typical intense vertical streak and a diffuse horizontal streak, while cracks could produce an intense vertical streak. Moreover, AFM could also enable to directly visualize the defects at the nanoscale,[16] which will be done in this study at the postmortem state.

Concerning pPLA, it was not clear if the plasticizer inclusions may deform or not upon drawing. To address this point, we conducted complementary μCT testing on a tensile specimen drawn at an engineering strain of 15%. The reconstructed images of a region taken in the necking where the whitening of the specimen was the most important is shown in Figure 8. At the nondeformed state [Fig. 8(a)], the material did not exhibit any contrast meaning that the density fluctuation between the plasticizer inclusions noted in Figure 2 and the PLA matrix was not important enough to be detected by μCT. After deformation, the inclusions became visible with a dark contrast [Fig. 8(b–d)] indicating a possible decrease of density upon drawing. In the 23-plane, oriented perpendicular to tensile direction [Fig. 8(b)], and in the 13-plane parallel to tensile direction corresponding to the tensile specimen thickness [Fig. 8(c)], no relevant information was noted. However, in the 12-plane, a relevant phenomenon was here noted. Some inclusions seemed to be positioned following lines oriented at ±45° from the tensile direction [Fig. 8(d)], which may be due to the propagation of shear bands from one inclusion to another.

Nanoscale Analysis of Deformation Heterogeneities

As described in the "Experimental" section, crazing exhibited a characteristic SAXS pattern and hence can be easily identified.[16,25,34] The correlation between tensile curves and time-resolved SAXS patterns of PLA upon drawing is represented in Figure 9. The typical scattering pattern of crazing was

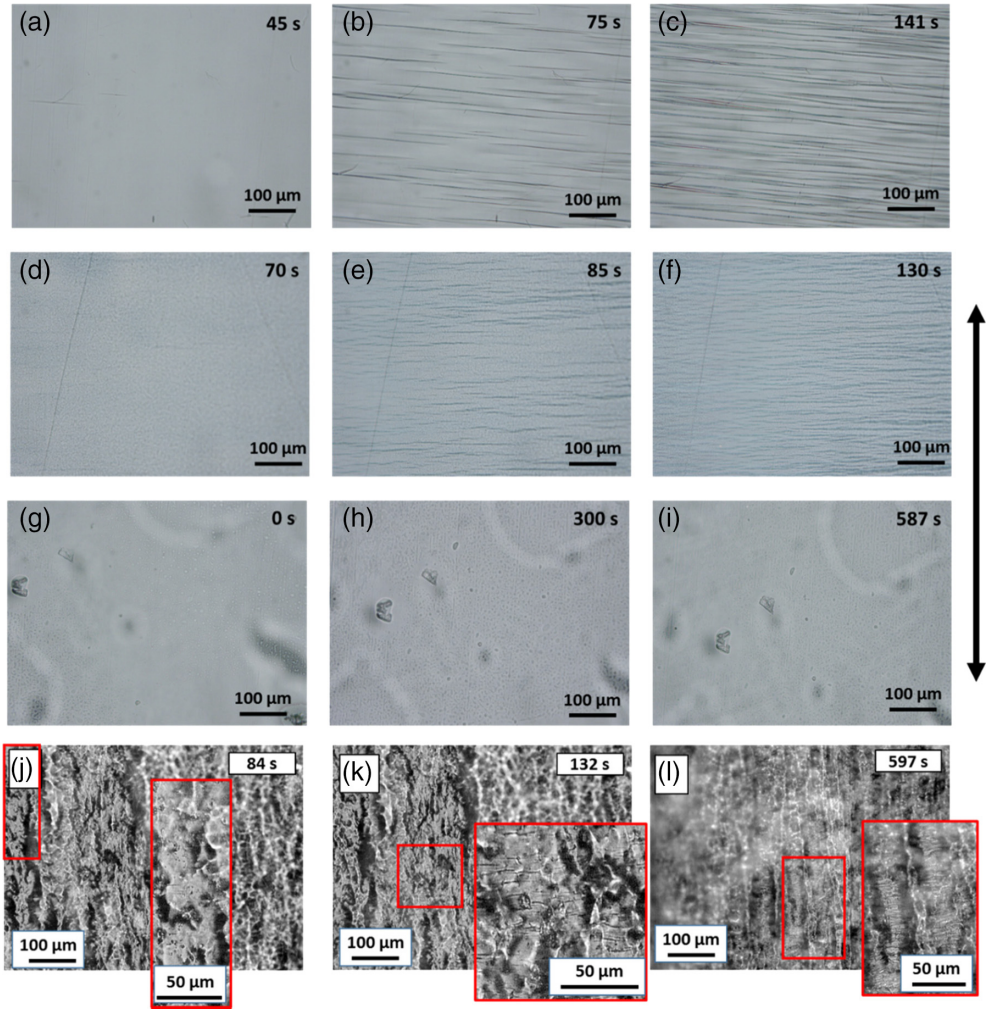

FIGURE 7 *In situ* optical microscope imaging of microscopic defects developing during the tensile testing of PLA (a)–(c), aPLA (d)–(f), PLA/acrylPEG (g)–(i), and pPLA (j)–(l), as a function of time (Tensile direction is indicated by the arrow). [Color figure can be viewed at wileyonlinelibrary.com]

observed from 20 s, consisting of (a) a meridian scattering streak due to the reflection of the craze walls and (b) an equatorial scattering streak due to the reflection of craze fibrils.[16,25] Therefore, contrary to the microscopic investigation of these defects where the formation of the crazes occurred just before the yield point [Figs. 6(a) and 7(a)], SAXS measurements clearly show that craze development occurred almost from the beginning of the tensile testing. It is also to be noted that meridian and equatorial scattering of crazing did not rigorously occur parallel and perpendicular to tensile direction, respectively, confirming that crazes are not perfectly oriented perpendicular to tensile direction as noted in Figure 7(b). The evolution of the equatorial invariant Q_{eq} and of the meridian invariant Q_{me} with time is plotted in Figure 9(a). It can be observed that both Q_{eq} and Q_{me} increased progressively with the imposed strain, and tended to stabilize just before the specimen breaking. This finding demonstrates that the volume fraction of the craze and of their internal fibrils increases with the deformation and stabilizes just before the breaking. Therefore, crazes are continuously formed during the drawing of PLA. It can be also noted that the invariant related to the craze wall scattering was much higher than the invariant related to the craze fibril scattering. Despite one craze contains an important volume fraction of fibrils, the low scattering engendered by the fibrils can be explained by an early break down of the fibrils limiting their number. It was observed that at a temperature below the glass transition of PLA (25 °C) and a strain rate of 0.01 s^{-1}, the yield stress was lower than the critical stress for the fibril break down,[16] which results in a fibril-break down before the yield point. The brittle behavior of PLA below its T_g is generally due to the loss of local ductility engendered by the craze fibrils breaking.

In the case of aPLA drawing, the recorded SAXS patterns at different times are represented in Figure 10. Almost no scattering was noted at 20 and 60 s, while a low meridian scattering was observed from 120 s in the viscoplastic stage [Fig. 6(a)]. This phenomenon was not attributed to crazing since the typical crazing scattering was not observed as for PLA [Fig. 9(d)], but could be attributed to the presence of cracks. So, our hypothesis relying on a possible hindering of the crazes by the crystalline

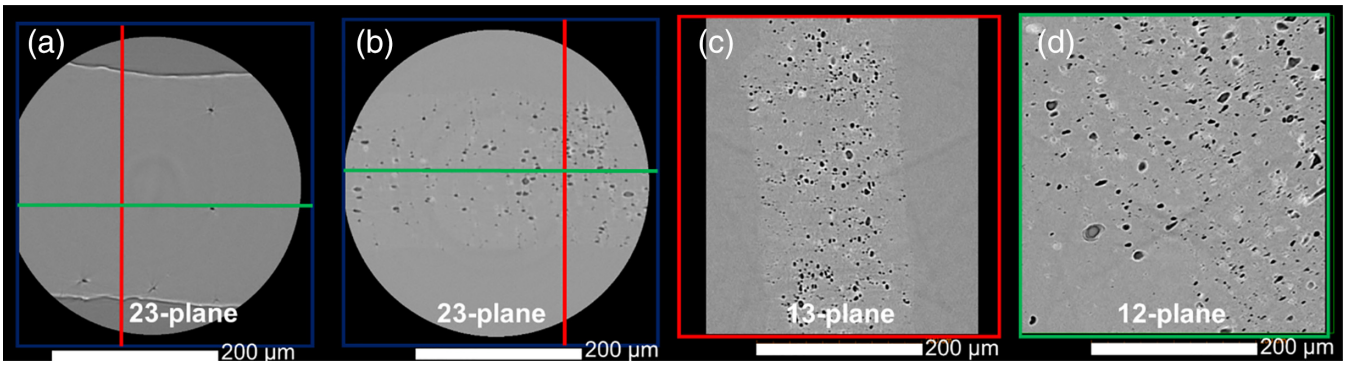

FIGURE 8 μCT reconstructed images of (a) an as-processed pPLA specimen and (b) to (d) a drawn specimen of pPLA at an engineering strain of 15% taken at the necking region, according to (a) and (b) 23-plane, (c) 13-plane, and (d) 12-plane (Axis 1 corresponds to the tensile direction). [Color figure can be viewed at wileyonlinelibrary.com]

lamellae is no longer valid in the case of aPLA. Further analysis is needed to identify the exact nature of the defects noted in aPLA [Figs. 7(d–f)]. Last, in the case of PLA/acrylPEG and pPLA, no scattering signal was observed by time-resolved SAXS proving that there is no crazing in these two plasticized PLAs, while the defects observed in pPLA at the microscale [Fig. 7(k,l)] did not surprisingly scatter X-rays.

To complement SAXS measurements, drawn specimens of PLA, aPLA, and pPLA were analyzed by AFM. In the case of PLA and aPLA, observations were conducted at the beginning of the defect area along tensile axis. The presence of crazes oriented perpendicular to tensile direction in the case of PLA was confirmed by the presence of fibrils bridging the defect lips as shown by the frequency contrast image [Fig. 11(e)]. In the case of aPLA, the defect morphology is quite different from the craze noted in PLA. If the depth of the defect is quite similar between PLA and aPLA [Fig. 11(c,d)], the defects in aPLA were tortuous [Fig. 11(b)], confirming optical microscope observations [Fig. 7(e)]. Furthermore, the defects seemed to have lateral branches [Fig. 11(b)]. When observing frequency contrast imaging in the case of aPLA, some sheaf-like spherulite residues were observed along the defects with a size of around 100 nm [Fig. 11(f)]. Despite having observed several specimens and numerous areas, it was not possible to visualize the spherulitic morphology of aPLA with a higher precision by AFM. It is thought that the defects in aPLA are generated from initial tribranch cracks present at the nuclei centers, as previously noted for PLA although the crystallization procedure differed from our study.[38,39] It is explained

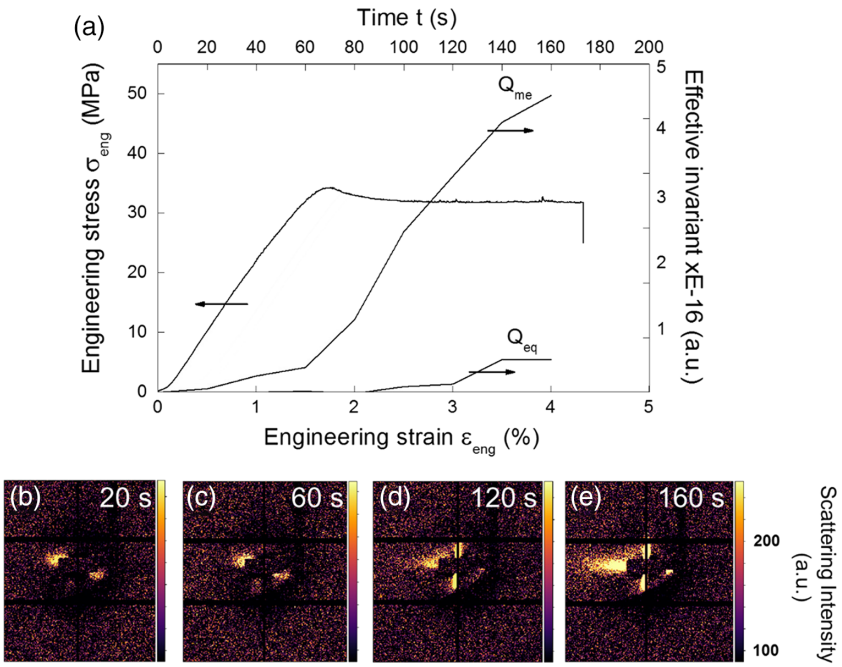

FIGURE 9 Tensile curve of PLA drawn at 20 °C and 2.7×10^{-4} s^{-1} (a), and recorded SAXS patterns at (b) 20 s, (c) 60 s, (d) 120 s and (e) 160 s (a.u. stands for arbitrary unit, tensile axis is vertical). [Color figure can be viewed at wileyonlinelibrary.com]

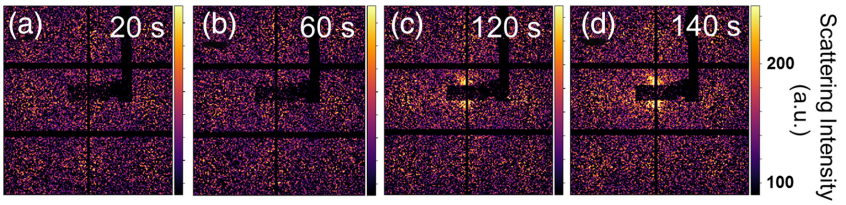

FIGURE 10 Recorded SAXS patterns at (a) 20 s, (b) 60 s, (c) 120 s, and (d) 140 s, during the drawing of aPLA at 20 °C and 2.7×10^{-4} s^{-1} (a.u. stands for arbitrary unit, tensile axis is vertical). [Color figure can be viewed at wileyonlinelibrary.com]

that such initial cracks are induced by thermal stress and contraction during the cooling procedure from the crystallization temperature to room temperature engendering directional differences in thermal expansion (CTE) in the PLA spherulites.[38] With drawing, these initial tribranch cracks may simply open preferentially along direction perpendicular to tensile direction. In the case of semicrystalline poly(4-methyl-1-pentene) (P4M1P) upon drawing below its T_g, it was reported that large crazes formed first in the amorphous regions between spherulites and then small crazes formed within the spherulites, this phenomenon being called two step cavitation.[3] aPLA that was also semicrystalline obviously not behaved as P4M1P, probably due to the presence of initial tribranch cracks preventing crazing. In the case of pPLA, the deformed sample exhibited an important roughness [Fig. 12(a, c)]. Three main features can be noted in the AFM imaging of this material: (a) the plasticizer inclusions, (b) shear bands bridging inclusions, and (c) defects oriented perpendicular to tensile direction. Such defects are most probably cracks and can be connected to shear bands [Fig. 12(a)] and plasticizer

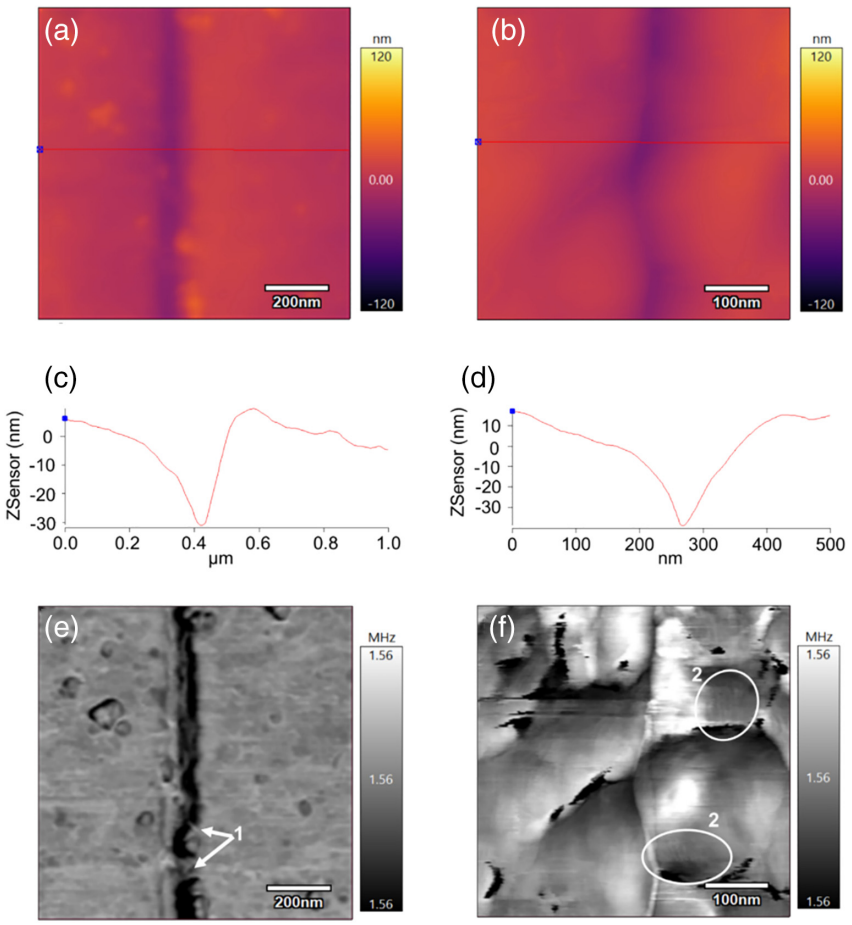

FIGURE 11 Postmortem AFM investigation of PLA (a), (c) and (e) at a strain of 3.8%, and aPLA (b), (d) and (f) at a strain of 4.1% observed with the topographical contrast mode (a) and (b) and the frequency contrast mode (subtle change in the MHz scale) (e) and (f). Note that some topographical profiles were represented in (c) and (d) (1: craze fibrils, and 2: possible sheaf-like spherulites, tensile axis is horizontal). [Color figure can be viewed at wileyonlinelibrary.com]

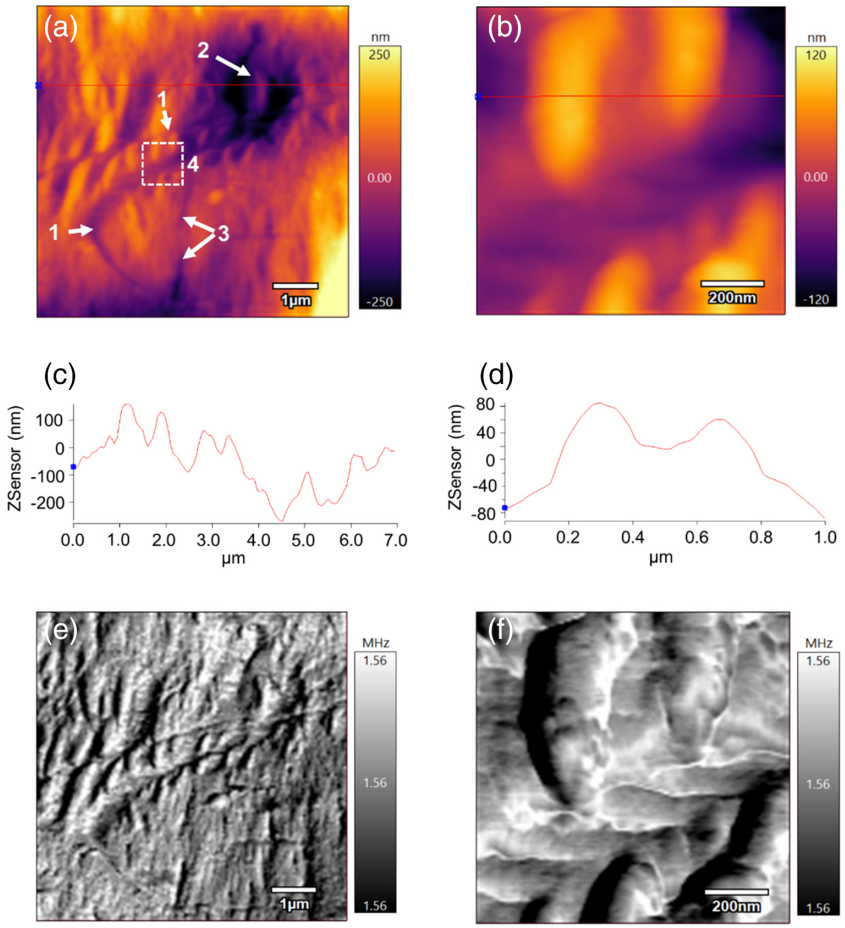

FIGURE 12 Postmortem AFM investigation of pPLA at a strain of 17.3% conducted with a low magnification (a) and (e), and with a high magnification (b) and (f), observed with the topographical contrast mode (a) and (b) and the frequency contrast mode (subtle change in the MHz scale) (e) and (f). Note that some topographical profiles were represented in (c) and (d) (1: shear bands, 2: inclusions, 3: cracks, and 4: area of the high magnification image, tensile axis is horizontal). [Color figure can be viewed at wileyonlinelibrary.com]

inclusions [Fig. 7(k)]. Note that images of shear bands recorded at a high magnification enabled to visualize their internal structure appearing as chevrons [Fig. 12(b,f)]. In our previous paper,[23] by STXM/NEXAFS we noted the presence of defects bridging the inclusions of pPLA that were attributed to cracks, which obviously is not the case based on the current AFM measurements.

Multiscale Correlation of Deformation Heterogeneities

It has only been possible to quantify deformation heterogeneities in PLA identified as crazing at the three scales of interest. So, a multiscale correlation between volume strain measured by DIC, craze surface density measured by optical microscopy and craze meridian invariant measured by SAXS was done. In particular, ε_v, S_d/S, and Q_{me} were normalized to their maximum values measured just before the specimen breaking, named ε_v^{max}, $(S_d/S)^{max}$ and Q_{me}^{max}, respectively, as represented in Figure 13. It can be noted that crazing quantification at the three scales had the same tendency as a function of time. In particular, normalized ε_v, S_d/S and Q_{me} increased slowly with time in the viscoelastic stage until 50 s, then in the viscoelastic stage they increased more rapidly. Interestingly, the detection of craze in the nanoscale started at about 20 s, while detection of craze at the microscopic scale started at about 45 s, meaning that crazes growing between these two scales took 25 s. Just after the yield point at 53 s, the normalized ε_v, S_d/S, and Q_{me} reached the same value of 0.1 indicating that roughly 90% of the craze development occurred during the viscoplastic stage. The knowledge provided here about crazing can be used to model damage in amorphous glassy polymers upon drawing by a physically based model. To go further, similar data could be obtained at different temperatures to increase experimental knowledge and modeling robustness of deformation heterogeneities.

Deformation Heterogeneities Related to the Initial PLA Structure

Our works clearly indicate that deformation heterogeneities depend on the physical and chemical structure of PLA. The identified deformation heterogeneities developing PLA, aPLA,

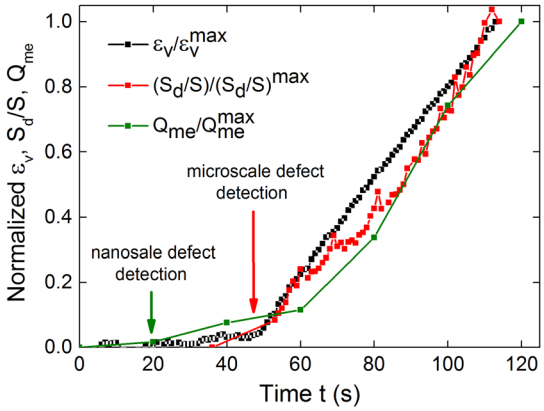

FIGURE 13 Multiscale correlation of craze characterization in PLA upon drawing at 20 °C and 2.7 × 10^{-4} s^{-1}. [Color figure can be viewed at wileyonlinelibrary.com]

PLA/acrylPEG, and pPLA upon drawing at room temperature are represented in Figure 14. Low crystalline PLA exhibited crazing explained by a high chain rigidity limiting chain mobility coupled with a high mass between entanglements providing a low molecular network resistance to deformation.[18,19] When submitting PLA to an annealing procedure, its crystallinity increased from 4.6 to 28.1 wt % (Table 1). Based on previous work, crystallization of PLA can engender initial tri-branch cracks present at the nuclei centers.[38] Drawing of such a material is expected to open the initial cracks without formation of craze since deformation is ensured by the opening of cracks before the sample breaking. The opening of existing

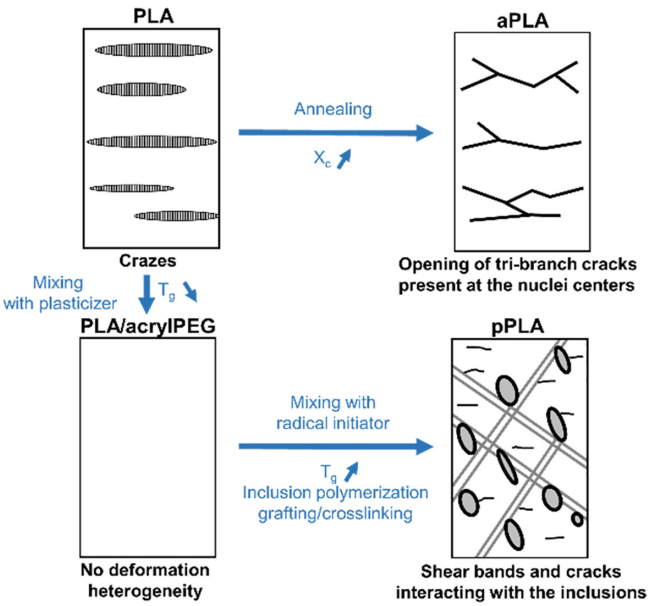

FIGURE 14 Schematic representation of deformation heterogeneities in PLA-based materials drawn in the plastic stage as a function of the treatment: annealing, blending with a plasticizer, and reactive blending with a plasticizer (Tensile axis is vertical). [Color figure can be viewed at wileyonlinelibrary.com]

defect may certainly require less mechanical energy than the creation of new ones, explaining a faster increase of surface defect density in the case of aPLA compared to PLA [Fig. 6 (a)]. The higher defect density in the case of aPLA may also explain why strain localization is less important in this material compared to PLA [Fig. 4(a,b)], as explained in previous works.[1] The plasticization of PLA by the physical blending with the acrylPEG plasticizer significantly increased chain mobility as indicated by the decrease of T_g from 62.5 to 11.4 °C (Table 1), so chain orientation mechanisms are enhanced and crazing is eliminated. However, the reactive plasticization yielded novel deformation heterogeneities that are shear bands and local cracks oriented perpendicular to tensile axis [Fig. 12(a)]. Shear bands exhibited an internal chevron-like morphology and propagated between neighboring inclusions. Under the effect of drawing and shear bands propagation, inclusions aligned along the shear bands [Fig. 8 (d)]. A decrease of inclusion internal density was also noted. The formation of cracks in pPLA was also observed in the matrix and at the inclusions level. Obviously, the presence of crosslinkings in pPLA may somewhat locally restrict the ability of the PLA chains to accommodate the macroscopic strain,[20,21] explaining the formation of shear bands. At high strain level, the rupture of these crosslinking points may occur inducing the formation of cracks at the inclusions-matrix interface and in the matrix [Figs. 7(k) and 12(a)]. Last, it is important to mention that local quantifications of deformation heterogeneity confirmed that the measurement of ε_v with our method is not precise, but only indicative of the dilatation tendency. Indeed, in the case of PLA/acrylPEG no defect formed upon drawing [Fig. 7(g–i)] while ε_v measurements indicated that this material reached a volume strain of about 0.02 [Fig. 3(b)], which was not consistent. Furthermore, the volume strains of PLA and aPLA were supposed to follow the same tendency [Fig. 3(b)], which was obviously not correct based on the microscopic investigations [Fig. 6(a)]. Our study highlights the importance to conduct multiscale structural investigations of polymeric materials when investigating their deformation heterogeneities.

CONCLUSIONS

The deformation heterogeneities in film samples of PLA-based materials were analyzed upon drawing by a multiscale and *in situ* approach. In particular, the impact of the initial crystallinity and two plasticization methodologies on deformation heterogeneities was carefully investigated.

In the case of low crystalline PLA (X_c = 4.6 wt % and T_g = 62.5 °C), crazing was identified by SAXS as deformation heterogeneity at the nanoscale. Crazing started almost at the beginning of the drawing and its volume fraction, proportional to the calculated meridian invariant, increased progressively with the imposed strain. At the microscopic scale, crazing was detected by optical microscopy just before the yield point and reached a surface density of 21.2% before the specimen breaking. Crazes were not rigorously oriented perpendicular to tensile direction, which was explained by specimen surface

defects at their edge engendering diagonal strain localization areas.

When increasing the initial PLA crystallinity from 4.6 to 28.1 wt % by an annealing procedure providing the material aPLA, crazing was not active (not detected by SAXS). Deformation heterogeneities involve defects forming from the yield point, whose surface density increased faster than for PLA reaching a higher value at the specimen breaking (29% vs. 21.2%). Moreover, defects in aPLA were tortuous and tended to coalesce. These defects were supposed to arise from the opening of initial tribranch cracks present at the nuclei centers. The higher defect density in aPLA compared to PLA could also be at the origin of the reduced strain localization, as shown by DIC.

The plasticization of PLA led to more ductile materials with a higher elongation compared to the reference PLA. In the case of the physical blend PLA/acrylPEG characterized by a glass transition temperature of 11.4 °C, no deformation heterogeneity was noted due to the high molecular mobility that can easily accommodates the imposed strain. In the case of the reactive plasticization of PLA with acrylPEG in the presence of a radical initiator, the resulting morphology had a drastic effect on deformation heterogeneities. Briefly, inclusions of polymerized plasticizer partially grafted to the matrix were noted, while the matrix was slightly crosslinked. Deformation heterogeneities in pPLA consisted of shear bands and cracks interacting with the inclusions. pPLA had a T_g of 36.4 °C indicating that its chain mobility is between that of PLA/acrylPEG and that of PLA, but its matrix rigidity is higher due to the presence of graftings/crosslinkings. The formation of shear bands instead of crazes in pPLA was hence explained by a higher chain mobility compared to PLA due to the presence of crosslinking points. The possible rupture of these crosslinking points may engender the formation of the observed cracks.

One important aspect that was not investigated here was the influence of temperature on the development of deformation heterogeneities, which is believed to provide novel knowledge on that topic.

ACKNOWLEDGMENTS

The authors acknowledge the Fonds National de la Recherche (FNR) Luxembourg for the grant of the FNR CORE project DuraPLA (C13/MS/5837188). The authors also thank Blank Holger, Volker Seybold, and Lars-Oliver Kautschor from Carl Zeiss Microscopy GmbH – Zeiss Group (Oberkochen, Germany) for the μCT testing. Thanks also go to Dr Inma Peral from the University of Luxembourg for her great help in preparing the SAXS/WAXS synchrotron application, as national contact point for large scale research instruments.

REFERENCES

1 C. G'Sell, J. M. Hiver, A. Dahoun, *Int. J. Solids Struct.* **2002**, *39*, 3857.

2 Y. Men, J. Rieger, J. Homeyer, *Macromolecules* **2004**, *37*, 9481.

3 R. Chen, Y. Lu, J. Zhao, Z. Jiang, Y. Men, *J. Polym. Sci. B* **2007**, *2016*, 54.

4 F. Addiego, A. Dahoun, C. G'Sell, J. M. Hiver, *Polymer* **2006**, *47*, 4387.

5 A. Pawlak, A. Galeski, A. Rozanski, *Prog. Polym. Sci.* **2014**, *39*, 921.

6 J. X. Li, W. L. Cheung, *Polymer* **1998**, *39*, 6935.

7 R. Hiss, S. Hobeika, C. Lynn, G. Strobl, *Macromolecules* **1999**, *32*, 4390.

8 B. Xiong, O. Lame, J. M. Chenal, C. Rochas, R. Séguéla, G. Vigier, *Macromolecules* **2015**, *48*, 5267.

9 F. Addiego, A. Dahoun, C. G'Sell, J. M. Hiver, O. Godard, *Polym. Eng. Sci.* **2009**, *49*, 1198.

10 M. Murariu, A. Da Silva Ferreira, M. Alexandre, P. Dubois, *Polym. Adv. Technol.* **2008**, *19*, 636.

11 A. C. Renouf-Glauser, J. Rose, D. F. Farrar, R. E. Cameron, *Biomaterials* **2005**, *26*, 5771.

12 X. C. Zhang, M. F. Butler, R. E. Cameron, *Polymer* **2000**, *41*, 3797.

13 G. Stoclet, R. Séguéla, J. M. Lefebvre, S. Elkoun, C. Vanmansart, *Macromolecules* **2010**, *43*, 1488.

14 G. Stoclet, R. Séguéla, J. M. Lefebvre, C. Rochas, *Macromolecules* **2010**, *43*, 7228.

15 G. Stoclet, R. Séguéla, C. Vanmansart, C. Rochas, J. M. Lefebvre, *Polymer* **2012**, *53*, 519.

16 G. Stoclet, J. M. Lefebvre, R. Séguéla, C. Vanmansart, *Polymer* **2014**, *55*, 1817.

17 A. S. Argon, M. M. Salama, *Philos. Mag.* **1977**, *36*, 1217.

18 C. A. P. Joziasse, H. Veenstra, D. W. Grijpma, A. J. Pennings, *Macromol. Chem. Phys.* **1996**, *197*, 2219.

19 D. W. Grijpma, J. P. Penning, A. J. Pennings, *Colloid Polym. Sci.* **1994**, *272*, 1068.

20 B. Brüster, F. Addiego, F. Hassouna, D. Ruch, J. M. Raquez, P. Dubois, *Polym. Degrad. Stab.* **2016**, *131*, 132.

21 G. Kfoury, F. Hassouna, J. M. Raquez, V. Toniazzo, D. Ruch, P. Dubois, *Macromol. Mater. Eng.* **2014**, *299*, 583.

22 K. Wang, B. Brüster, F. Addiego, G. Kfoury, F. Hassouna, D. Ruch, J. M. Raquez, P. Dubois, *Polym. Int.* **2015**, *64*, 1544.

23 B. Brüster, C. Amozoqueño, P. Grysan, I. Peral, B. Watts, J. M. Raquez, P. Dubois, F. Addiego, *Macromol. Mater. Eng.* **2017**, *302*, 1700326.

24 E. W. Fischer, H. J. Sterzel, G. Wegner, Z. Z. Kolloid, *Polymer* **1973**, *251*, 980.

25 B. J. P. Jansen, S. Rastogi, H. E. H. Meijer, P. J. Lemstra, *Macromolecules* **2001**, *34*, 4007.

26 N. Stribeck, In *X-Ray Scattering of Soft Matter*, H. Pasch Ed., Springer-Verlag, Berlin, **2007**.

27 G. J. Salomons, M. A. Singh, T. Bardouille, W. A. Foran, M. S. Capel, *J. Appl. Cryst.* **1999**, *32*, 71.

28 F. Addiego, S. Patlazhan, K. Wang, S. André, S. Bernstorff, D. Ruch, *Polym. Int.* **2015**, *64*, 1513.

29 L. Farge, S. André, F. Meneau, J. Dillet, C. Cunat, *Macromolecules* **2013**, *46*, 9659.

30 K. Choi, M. C. Choi, D. H. Han, T. S. Park, C. S. Ha, *Eur. Polym. J.* **2013**, *49*, 2356.

31 J. Gámez-Pérez, J. C. Velazquez-Infante, E. Franco-Urquiza, P. Pages, F. Carrasco, O. O. Santana, M. L. Maspoch, *eXPRESS Polym. Lett.* **2011**, *5*, 82.

32 T. E. Brady, G. S. Y. Yeh, *J. Mater. Sci.* **1973**, *8*, 1083.

33 K. M. Choi, S. W. Lim, M. C. Choi, Y. M. Kim, D. H. Han, C. S. Ha, *Polym. Bull.* **2014**, *71*, 3305.

34 X. Zhang, K. Schneider, G. Liu, J. Chen, K. Brüning, D. Wang, M. Stamm, *Polymer* **2012**, *53*, 648.

35 F. Rezgui, M. Swistek, J. M. Hiver, C. G'Sell, T. Sadoun, *Polymer* **2005**, *46*, 7370.

36 A. I. Leonov, *Int. J. Solids Struct.* **2002**, *39*, 5913.

37 H. X. Li, C. P. Buckley, *Int. J. Solids Struct.* **2009**, *46*, 1607.

38 E. M. Woo, G. Lugito, *Polymers* **2016**, *8*, 329.

39 C. Fraschini, R. Plesu, J. R. Sarasua, R. E. Prud'homme, *J. Polym. Sci. B* **2005**, *43*, 3308.